

Mobility edge and multifractality in a periodically driven Aubry-André model

Madhumita Sarkar, Roopayan Ghosh, Arnab Sen, and K. Sengupta
School of Physical Sciences, Indian Association for the Cultivation of Science,
2A and 2B Raja S. C. Mullick Road, Jadavpur 700032, India
(Dated: February 25, 2021)

We study the localization-delocalization transition of Floquet eigenstates in a driven fermionic chain with an incommensurate Aubry-André potential and a hopping amplitude which is varied periodically in time. Our analysis shows the presence of a mobility edge separating single-particle delocalized states from localized and multifractal states in the Floquet spectrum. Such a mobility edge does not have any counterpart in the static Aubry-André model and exists for a range of drive frequencies near the critical frequency at which the transition occurs. The presence of the mobility edge is shown to leave a distinct imprint on fermion transport in the driven chain; it also influences the Shannon entropy and the survival probability of the fermions at long times. In addition, we find the presence of CAT states in the Floquet spectrum with weights centered around a few nearby sites of the chain. This is shown to be tied to the flattening of Floquet bands over a range of quasienergies. We support our numerical studies with a semi-analytic expression for the Floquet Hamiltonian (H_F) computed within a Floquet perturbation theory. The eigenspectra of the perturbative H_F so obtained exhibit qualitatively identical properties to the exact eigenstates of H_F obtained numerically. Our results thus constitute an analytic expression of a H_F whose spectrum supports multifractal and CAT states. We suggest experiments which can test our theory.

I. INTRODUCTION

Localization phenomenon in an one-dimensional (1D) fermion chain with quasiperiodic potentials has been studied extensively in the past¹⁻⁴. These studies have received a new impetus in recent times due to experimental realization of such potentials in ultracold atom chains^{5,6}. In contrast to the more conventional models with uncorrelated disorder which exhibits such localization for any disorder strength in 1D⁷, fermion chains with non-random but quasiperiodic potentials harbor a localization-delocalization transition^{1,2}. The simplest of such models termed as Aubry-André (AA) model¹ has an Hamiltonian given by $H = H_k + H_p$ where

$$H_k = -\frac{\mathcal{J}}{2} \sum_j c_j^\dagger (c_{j+1} + c_{j-1})$$
$$H_p = \sum_j V_0 \cos(2\pi\eta j + \phi) c_j^\dagger c_j. \quad (1)$$

Here j is the site index of the chain, c_j denotes fermionic annihilation operator at site j , \mathcal{J} is the hopping amplitude, η is an irrational number usually chosen to be the golden ratio $(\sqrt{5} - 1)/2$, V_0 is the amplitude of the potential, and ϕ is an arbitrary global phase. The AA Hamiltonian can be shown to be self-dual and hosts a localization-delocalization transition at $V_{0c} = 2\mathcal{J}$ ¹. For $V_0 > (<)V_{0c}$, all the single-particle states in the spectrum for the model are localized (delocalized). Such transitions also occur in models with a more general class of such quasiperiodic potentials (termed as generalized Aubry-André (GAA) potentials). These GAA Hamiltonians may have several forms; for example, they may be given by Eq. 1 with a different form of the quasiperiodic potential $[\cos(2\pi\eta j + \phi) \rightarrow \cos(2\pi\eta j + \phi)/(1 - \alpha \cos(2\pi\eta j + \phi))]$ ² or with longer range hopping $\mathcal{J} \rightarrow \mathcal{J}_{ij} = \mathcal{J}/|i - j|^a$,

where a is an exponent³. One of the key aspects of these GAA Hamiltonians which is absent in the AA model is the presence of a mobility edge in the spectrum. Moreover, the latter class of GAA models also host band of multifractal eigenstates in the delocalized phase. These states, unlike their delocalized counterpart, are non-ergodic; thus their presence change the ergodicity properties of these models³.

The study of non-equilibrium dynamics of closed quantum systems has gained tremendous impetus in the last decade^{8,9}. More recently, it was realized that periodically (or quasiperiodically) driven systems host a wide range of interesting phenomena that have no analog in their undriven counterparts. These include topological transitions in driven systems¹⁰, dynamical transitions^{11,12}, dynamical freezing^{13,14}, realization of time crystals^{15,16}, and weak ergodicity breaking behavior¹⁷. Moreover such driven systems are known to lead to novel steady states which have no analog in non-driven systems^{18,19}. For periodically driven systems, most of these phenomena can be understood by analyzing its Floquet Hamiltonian H_F which is related to the evolution operator via $U(T, 0) = \exp[-iH_F T/\hbar]$ ²⁰, where $T = 2\pi/\omega_D$ is the drive period, ω_D is the drive frequency, and \hbar is the Planck's constant.

In this work, we study the properties of the Floquet eigenstates of a driven fermionic chain in the presence of an AA potential. The Hamiltonian of the chain that we study is given by Eq. 1 with $\mathcal{J} \rightarrow \mathcal{J}(t)$, where $\mathcal{J}(t)$ is a periodic function of time characterized by a drive frequency ω_D . In our study, we choose two distinct protocols for $\mathcal{J}(t)$. The first is the square pulse protocol where $\mathcal{J}(t) = \mathcal{J}_0(-\mathcal{J}_0)$ for $t \leq (>)T/2$ while the second is continuous protocol for which $\mathcal{J}(t) = \mathcal{J}_0 \cos \omega_D t$. For both these protocols, we choose $\mathcal{J}_0 \gg V_0$. In the regime, of large drive frequency, $H_F \simeq H_p$, so that all

the Floquet states are localized. In contrast, for quasistatic drive $\omega_D \simeq 0$, all the states are expected to be delocalized since $\mathcal{J}_0 \gg V_0$. This feature ensures the presence of a localization-delocalization transition in the Floquet spectrum; the aim of the present work is to understand the nature of the Floquet eigenstates near the transition. We carry out this analysis numerically using exact diagonalization of the fermionic chain followed by numerical computation of $U(T, 0)$; this numerical study is complemented by a semi-analytic, albeit perturbative, computation of H_F using a Floquet perturbation theory (FPT)^{21,22}.

The central results that we obtain from this analysis are as follows. First, we find that for a range of drive frequencies around the localization-delocalization transition (occurring at a critical value of the drive frequency ω_c), the Floquet spectrum of the driven AA model supports a mobility edge. This mobility edge, which has no analog in the static AA model, occurs for $\omega_D \leq \omega_c$ and separates the delocalized states from either localized or multifractal band of states. We chart out the drive frequency range for which these multifractal states are present for both the square-pulse and continuous drive protocols. Second, we unravel the presence of single-particle CAT states in the Floquet spectrum for $\omega_D \geq \omega_c$. These states occur at two specific quasienergies in the Floquet spectrum and have wavefunctions which are localized around two or three next-nearest neighbor sites in the chain. We tie the presence of these states to the presence of near-flat band dispersion in the Floquet spectrum at these quasienergies and provide a semi-analytic understanding of their existence. Third, we study the transport in such driven chain by tracking the steady state value of the fermion density as a function of drive frequency starting from a domain-wall initial state. This initial state constitutes a many-body state where all sites to the left (right) of the chain center are occupied (empty). The density of the fermions in the steady state stays close to its initial profile in the localized phase; in contrast it evolves to an uniform density profile for the delocalized phase. In between, near the transition where the mobility edge exists, it shows an intermediate behavior which arises from the presence of both delocalized and localized (or multifractal) states in the Floquet spectrum. Analogous features are found in the Shannon entropy, and the return probability of a single-particle fermion wavefunction (initially localized at the center of the chain) measured in the steady state. Fourth, we construct a semi-analytic, albeit perturbative, expression of the Floquet Hamiltonian H_F using a FPT. We show that this semi-analytic Hamiltonian qualitatively captures the physics of the driven system and use it to explain the presence of the mobility edge and the multifractal states in the Floquet spectrum. Finally, we discuss possible experiments which can test our theory.

The plan of the rest of the paper is as follows. In Sec. II, we provide a detailed numerical study of the driven chain charting out the phase diagram, demonstrating the

existence of the mobility edge, and determining the location of the multifractal and CAT states. This is followed by Sec. III where we construct a semi-analytic Floquet Hamiltonian using FPT. Finally, we summarize our main results and suggest experiments which can test our theory in Sec. IV. Some details of the calculation of H_F and a discussion of the approach of the driven chain to the steady state are presented in the Appendices.

II. NUMERICAL RESULTS

In this section, we present exact numerical result on the driven fermion chain for both square-pulse (Sec. II A) and sinusoidal drive protocol (Sec. II B). Henceforth, we set the global phase $\phi = 0$ in Eq. 1 without loss of generality.

A. Square pulse protocol

For the square-pulse protocol, we vary the hopping amplitude of the AA model (Eq. 1) as

$$\begin{aligned} \mathcal{J}(t) &= -\mathcal{J}_0, & t \leq T/2 \\ &= \mathcal{J}_0, & t > T/2 \end{aligned} \quad (2)$$

This protocol is chosen to ensure that at the high frequency limit where $H_F \simeq \int_0^T H(t)dt/T = H_p$, the Floquet Hamiltonian represents a localized phase. To numerically find out the Floquet spectrum at arbitrary frequency, we first find the eigenspectrum of $H_{\pm} = H[\pm\mathcal{J}_0]$ (Eq. 1) using exact diagonalization (ED). We denote these eigenvalues and eigenvectors as ϵ_m^{\pm} and $|\psi_m^{\pm}\rangle$ respectively. Next, we note that for the protocol given by Eq. 2, the evolution operator at $t = T$ can be written as

$$\begin{aligned} U(T, 0) &= e^{-iH_+T/(2\hbar)} e^{-iH_-T/(2\hbar)} \\ &= \sum_{p^+, q^-} e^{i(\epsilon_p^+ - \epsilon_q^-)T/(2\hbar)} c_{p^+q^-} |\psi_p^+\rangle \langle \psi_q^-| \end{aligned} \quad (3)$$

where the coefficients $c_{p^+q^-} = \langle \psi_p^+ | \psi_q^- \rangle$ denote overlap between the two eigenbasis. Next, we numerically diagonalize $U(T, 0)$ and obtain its eigenvalues λ_m and $|\psi_m\rangle$. The corresponding eigensternum of H_F is then obtained using the relation $U(T, 0) = \exp[-iH_FT/\hbar]$ which identifies the eigenvectors of $U(T, 0)$ and H_F and yields

$$U(T, 0) = \sum_m \lambda_m |\psi_m\rangle \langle \psi_m|, \quad \lambda_m = e^{-i\epsilon_m^F T/\hbar} \quad (4)$$

where ϵ_m^F are the quasienergies which satisfy $H_F|\psi_m\rangle = \epsilon_m^F|\psi_m\rangle$. In this section, we shall use the properties of these Floquet eigenvalues and eigenvectors to study phase diagram of the driven chain along with multifractality of Floquet eigenstates and transport of fermions.

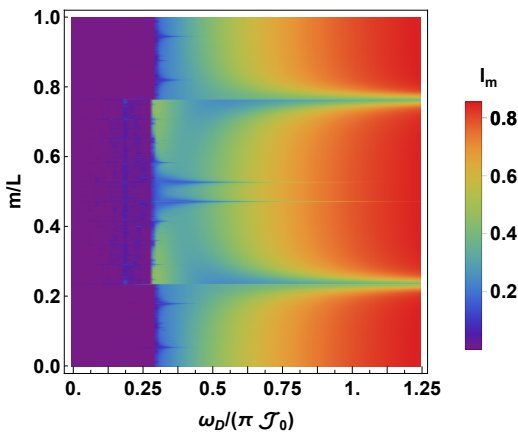


FIG. 1: Plot of I_m as a function of the normalized eigenfunction index m/L and $\omega_D/(\pi\mathcal{J}_0)$ showing the localized/delocalized nature of the Floquet eigenstates $|\psi_m\rangle$. Here $L = 2048$ and we have set $\mathcal{J}_0 = 1$, $V_0/\mathcal{J}_0 = 0.05$, and scaled all energies (frequencies) in units of $\mathcal{J}_0(\mathcal{J}_0/\hbar)$.

1. Phase diagram and CAT states

Having obtained the eigenspectrum of H_F , we first analyze the localization properties of normalized single-particle eigenstates $|\psi_m\rangle$ as a function of the drive frequency. To this end, we compute the inverse participation ratio (IPR) of these states given by

$$I_m = \sum_{j=1}^L |\psi_m(j)|^4, \quad \psi_m(j) = \langle j | \psi_m \rangle \quad (5)$$

where j denotes the coordinate of the lattice sites of the chain of length L . The IPR $I_m \sim L^{-1(0)}$ in $d = 1$ for a delocalized (localized) state and thus acts as a measure of localization of a quantum state.

This analysis leads to the phase diagram shown in Fig. 1, where we present I_m as a function of the drive frequency ω_D and for $V_0/\mathcal{J}_0 = 0.05$. As expected, the Floquet eigenstates stay localized at large drive frequency; in contrast, they are delocalized at low drive frequencies. In between, around $\hbar\omega_D/\mathcal{J}_0 \simeq 0.3\pi$, we find a localization-delocalization transition. Near the transition, for drive frequencies $0.15\pi \leq \hbar\omega_D/\mathcal{J}_0 \leq 0.3\pi$, we find the existence of a mobility edge separating a delocalized band hosting states with $I_m \simeq 1/L \leq 10^{-3}$ from those with finite $I_m > 0.1$. The nature of the states separated by this mobility edge will be analyzed in detail in the next subsection.

In addition to the mobility edge near the transition, we also find a two narrow bands of states which retain a smaller value of $I_m \simeq 0.5$ deep inside the localized phase. In what follows, we analyze the character of these states. First, a plot of $|\psi_m(j)|^2$ at a fixed frequency ω_D , shown in the top panels of Fig. 2, reveals that these states have their weights spread between few lattice sites even deep inside the localized phase. This behavior is to be

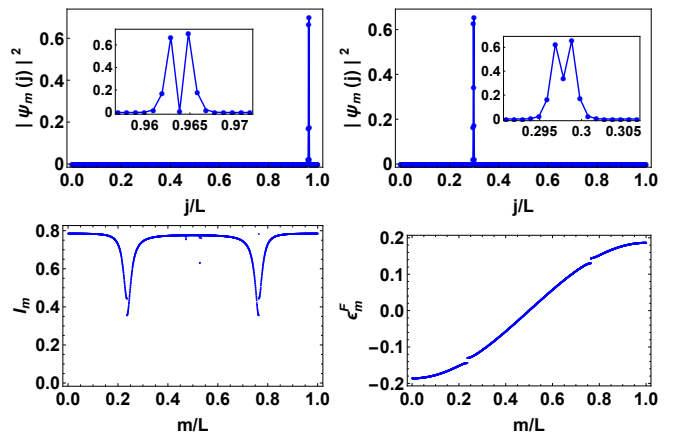


FIG. 2: Top Panels: Spatial distribution of the CAT states at $m/L = 0.24$ (left panel) and $m/L = 0.76$ (right panel) and $\omega_D/(\pi\mathcal{J}_0) = 1$. Bottom left panel: Plot of I_m as a function of m/L showing the dip in I_m for the CAT states. Bottom right panel: Plot of ϵ_m^F as a function of m/L at the same frequency showing flattening of Floquet bands before the gap near $m/L \simeq 0.24, 0.76$. All other parameters are as in Fig. 1. See text for details.

contrasted with that of a canonical localized state where $|\psi_m(j)|^2$ is finite only on a single site. This feature makes them perfect examples of CAT states whose wavefunctions are localized over more than one site. These states can also be distinguished from either localized or delocalized states via I_m . This can be clearly seen in the bottom left panel of Fig. 2 where one sees a clear dip in I_m for these states. The reason for the existence of such states can be understood from the structure of the Floquet eigenenergies ϵ_m^F shown in the bottom right panel of Fig. 2 for $\hbar\omega_D/\mathcal{J}_0 = \pi$ deep inside the localized regime. The Floquet energy dispersion becomes flat near the gaps in the spectrum; we have checked that this characteristic persists for all $\omega \geq \omega_c$ for large enough L . We find that the CAT states reside in these flat band regimes of the Floquet spectrum.

The existence of such CAT states and its relation to the flat regions in the Floquet band can be understood, in the high frequency regime, as follows. We first note that in this regime, from the first order Magnus expansion $H_F \simeq H_p$; thus H_F is almost diagonal in the position basis; each of its eigenstates is localized on one of the sites and these eigenstates can be approximately labeled by site indices of the chain. The off-diagonal terms are generated at higher order in the Magnus expansion and are therefore typically small in this region. Usually if the quasienergies are well-separated from each other, these off-diagonal terms do not change the nature of the Floquet spectrum. However, we note that this assumption breaks down around $m/L \simeq 0.24, 0.76$; the quasienergy spacing between the states localized in this regime approaches zero as can be seen from flattening of the Floquet band. Consequently, the presence of off-diagonal term in H_F arising from H_K , however small, becomes

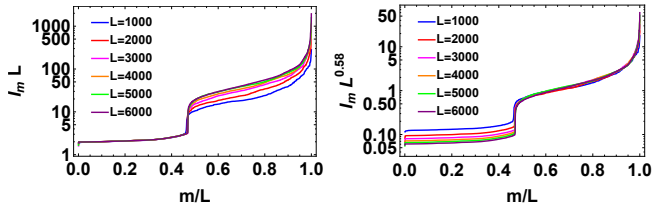


FIG. 3: Left Panel: Plot of $I_m L$ as a function of m/L (sorted in increasing order of I_m) for $\omega_D/(\pi \mathcal{J}_0) = 0.245$ for several L showing collapse of the delocalized states below the mobility edge around the middle of the spectrum. Right panel: Similar plot for $I_m L^{0.58}$ showing collapse of the multifractal states above the mobility edge. All other parameters are same as in Fig. 1.

important and leads to hybridization of the states localized on nearby sites. This leads to a pair of CAT states in the spectrum. We note that these states persists only for frequencies where the Floquet spectrum has a flat region; for $\omega_D \leq \omega_c$, this feature is absent and one does not find the CAT states in this regime.

2. Multifractal states

The multifractal nature of a quantum state can not be ascertained from the IPR alone. To this end, we now present computation of a generalized IPR defined as^{23,24}

$$I_m^{(q)} = \sum_{j=1}^L |\psi_m(j)|^{2q} \quad (6)$$

where $I_m \equiv I_m^{(2)}$. It is well-known that $I_m^{(q)} \sim L^{-\tau_q}$, where the fractal dimension of the state is given by $D_q = \tau_q/(q-1)$. We note that for delocalized states $D_q = 1$ for all q , while for localized states $D_q = \tau_q = 0$. Multifractal states typically yield $0 < D_q < 1$.

From the phase diagram shown in Fig. 1, it can be seen that the Floquet eigenstates are mostly perfectly localized for large $\omega_D \gg \omega_c$; in contrast, they are delocalized for $\omega_D \simeq 0$. Thus it is evident that the presence of multifractal states, if any, would be near the transition where the mobility edge separates delocalized states from a bunch of states for which $0 < \tau_2 < 1$. With this expectation, we first plot I_m for all Floquet eigenstates near the transition corresponding to $\hbar\omega_D/\mathcal{J}_0 = 0.245\pi$ in Fig. 3 after sorting the eigenstates in terms of increasing IPR, which clearly shows the presence of delocalized states and multifractal states separated by a mobility edge. The left panel shows a plot of $I_m L$ for all states; we find that for the states with $m/L < 0.6$, this quantity collapses for the different system sizes indicating that $I_m \sim L^{-1}$ and hence, the delocalized nature of these states. In contrast, the right panel of the Fig. 3 indicates that I_m for all states with $m/L > 0.6$ scale as $L^{-0.58}$ indicating $\tau_2 = D_2 = 0.58$ and a multifractal nature. To confirm this, we plot $I_m^{(q)}$ for these states for $q = 3$ and $q = 4$ as

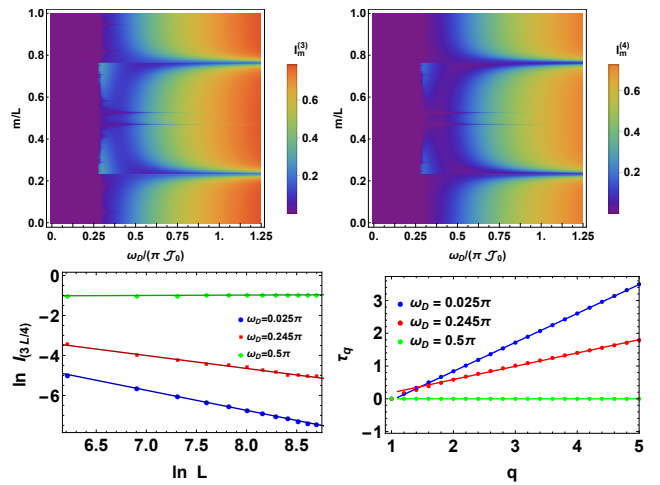


FIG. 4: Top Panels: Plot of $I_m^{(3)}$ (left panel) and $I_m^{(4)}$ (right panel) as a function of m/L and ω_D indicating multifractal states at intermediate frequency. Bottom left panel: Plot for $\ln I_m$ vs $\ln L$ used for extracting τ_2 for several representative frequencies for the state corresponding to $m/L = 0.75$. The behavior of perfectly delocalized (blue dots at $\omega_D/(\pi \mathcal{J}_0) = 0.025$) and localized (green dots, $\omega_D/(\pi \mathcal{J}_0) = 0.5$) can be distinguished from that of a multifractal states (red dots $\omega_D/(\pi \mathcal{J}_0) = 0.245$). Bottom right panel: Plot of τ_q as a function of q for a delocalized (blue dots at $\omega_D/(\pi \mathcal{J}_0) = 0.025$), localized (green dots at $\omega_D/(\pi \mathcal{J}_0) = 0.5$) and multifractal (red dots at $\omega_D/(\pi \mathcal{J}_0) = 0.245$) states. All other parameters are same as in Fig. 1.

shown in top panels of Fig. 4. The value of τ_q is extracted from a plot of $\ln I_m^{(q)}$ vs $\ln L$ for several L as shown in the bottom left panel of Fig. 4, where $m/L \approx 3/4$ after sorting in increasing order of I_m for each L . A plot of τ_q obtained using this procedure is shown as a function q for representative drive frequencies in the right bottom panel of Fig. 4. We find that $\tau_q \sim D_q(q-1)$ for all plots; $D_q \sim 0(1)$ for localized (delocalized) states corresponding to $\hbar\omega_D/\mathcal{J}_0 = 0.5(0.025)\pi$ while $0 < D_q < 1$ for multifractal states at $\hbar\omega_D/\mathcal{J}_0 = 0.245\pi$.

Numerically we find the presence of multifractal states for a wide range of frequencies below ω_c , till $\hbar\omega_D/\mathcal{J}_0 = 0.15\pi$. This is shown in the left panel of Fig. 5 where we plot τ_q for all states in the Hilbert space after sorting in increasing order of I_m as a function of ω_D . This clearly shows the presence of multifractal states with quasienergies higher than the mobility edge for $0.15\pi \leq \hbar\omega_D/\mathcal{J}_0 \leq 0.25\pi$. Our analysis indicates that the multifractal dimension D_q is a non-monotonic function of ω_D . This is shown in the right panel of Fig. 5 for a randomly chosen state corresponding to $m/L = 0.75$. The dip in the plot around $\hbar\omega_D/\mathcal{J}_0 = 0.2\pi$ corresponds to the narrow frequency region where we find localized, rather than multifractal, states above the mobility edge.

Another test of multifractality of a given state is the distribution of the energy difference between the odd-even ($s_m^{\text{o-e}} = \epsilon_{2m+1}^F - \epsilon_{2m}^F$) and the even-odd ($s_m^{\text{e-o}} =$

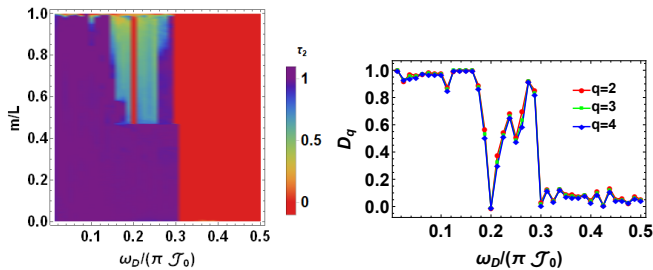


FIG. 5: Left: Plot of τ_2 as a function of m/L (after sorting in increasing order of I_m) and $\omega_D/(\pi\mathcal{J}_0)$ showing the mobility edge separating delocalized and multifractal states for $0.15 \leq \omega_D/(\pi\mathcal{J}_0) \leq 0.25$. The system sizes used for extracting τ_2 are $L = 500, \dots, 6000$ in steps of 500. Right: Plot of D_q as a function of $\omega_D/(\pi\mathcal{J}_0)$ for $m/L = 0.75$. All other parameters are same as in Fig. 1. See text for details.

$\epsilon_{2m}^F - \epsilon_{2m-1}^F$) energies³. For delocalized states these two gaps are different due to almost doubly degenerate spectrum leading to $s_m^{o-e} \simeq 0$ while for the localized states, this distinction is not present, hence this gap vanishes. For multifractal states, the behavior follows neither of the two patterns and both s_m^{o-e} and s_m^{e-o} show a scattered behavior. Thus one can distinguish between different set of states by studying these energy gaps.

In our case, due to the drive, we study the difference of quasi-energies. Since our spectrum has a mobility edge, the quasi-energy spectrum is folded.²⁵ There is no general way to unfold the spectrum in such a case; consequently, the identification of odd and even energies cannot be done uniquely at low and intermediate drive frequencies. However, the distribution of quasi-energy differences would still show the same features as discussed in the last paragraph. Hence to highlight the expected behavior, we define two new quantities, $s_m^{min} = \text{Min}[s_m^{o-e}, s_m^{e-o}]$ and $s_m^{max} = \text{Max}[s_m^{o-e}, s_m^{e-o}]$, which would allow us to separate the two gaps properly in the delocalized region of the spectrum.

A plot of $\ln s_m^{min}$ and $\ln s_m^{max}$ is shown in Fig. 6 as a function of m/L for several representative frequencies. For $\hbar\omega_D/\mathcal{J}_0 = 0.025\pi$, where all states are delocalized, the plot shows clear separation of these two quantities for all m/L ; we find, in accordance to standard expectation, that $s_m^{min} \simeq 0$ for all m . In contrast for $\hbar\omega_D/\mathcal{J}_0 = 0.5\pi$, where all states are localized we find regular distribution of both energy gaps as shown in the bottom right panel of Fig. 6. The small difference between s_m^{min} and s_m^{max} in this regime is a finite size effect and reduces with increasing L . In contrast, in the intermediate frequency regime at $\hbar\omega_D/\mathcal{J}_0 = 0.175\pi$ (top right panel of Fig. 6), we find clear signature of a mobility edge separating delocalized and multifractal states; the latter class of states can be recognized by strong scattering in distribution of both $\ln s_m^{min}$ and $\ln s_m^{max}$ ³. The presence of a mobility edge separating the localized and delocalized at $\hbar\omega_D/\mathcal{J}_0 = 0.2\pi$ is shown in the bottom left panel of Fig. 6. We find that the presence of localized states

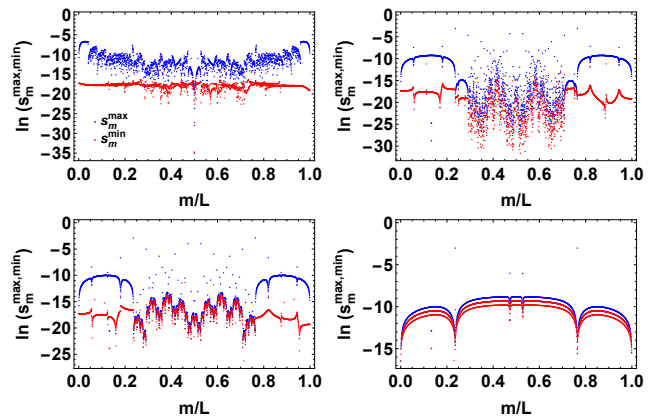


FIG. 6: Top Panels: Plot of $\ln s_m^{min}$ (red dots) and $\ln s_m^{max}$ (blue dots) as a function of m/L for $\omega_D/(\pi\mathcal{J}_0) = 0.025$ (top left panel), 0.175 (top right panel), 0.2 (bottom left panel), and 0.5 (bottom right panel). We have set $L = 4181$, since L needs to be a Fibonacci number. All other parameters are same as in Fig. 1.

above the mobility edge can be clearly distinguished from that of multifractal states because here there is a overlap of $\ln s_m^{min}$ and $\ln s_m^{max}$ unlike the scattered distribution found in the latter states.

Before ending this subsection, we would like to point out that our analysis shows that the driven AA model, at intermediate frequencies, shows mobility edge and multifractal states even when the parent Hamiltonian (Eq. 1) does not host either of these features. This distinguishes this phenomenon from earlier studies of driven GAA model where the drive, in the high frequency regime, creates a multifractal state by superposing localized and delocalized states across the mobility edge of the static GAA Hamiltonian²⁶. For completeness, we note here that Ref. 27 showed that periodic modulations of the phase of the hopping amplitude (e.g., by applying a time dependent gauge field) in the AA model also exhibited a mobility edge and multifractal states. However, in our case, the time dependent hopping amplitudes are real-valued. The mechanism leading to the multifractal states for the driven AA model shall be discussed in Sec. III.

3. Transport, return probability and entropy

In this subsection, we address the effect of the presence of mobility edge on fermion transport, survival probability of the fermion wavefunction in the steady state and their Shannon entropy .

For studying transport property of the fermions we start from a domain-wall initial state²⁸ defined, in the fermion number basis, by

$$|\psi_{\text{init}}\rangle = |n_1 = 1, \dots, n_{L/2} = 1, n_{L/2+1} = 0, \dots, n_L = 0\rangle \quad (7)$$

where we have taken L to be an even integer (chain with even number of sites) and $n_j = \langle \hat{n}_j \rangle$ denotes fermion

occupation number on the j^{th} site and $\hat{n}_j = c_j^\dagger c_j$ is the fermion number operator on that site. The wavefunction after n drive cycles is then given by

$$|\psi'\rangle = U(nT, 0)|\psi_{\text{init}}\rangle = \sum_m c_m^{\text{init}} e^{-in\epsilon_m^F T/\hbar} |\psi_m\rangle \quad (8)$$

where $|\psi_m\rangle$ denotes Floquet eigenstates with $L/2$ fermions and $c_m^{\text{init}} = \langle\psi_m|\psi_{\text{init}}\rangle$. Using this state, one may compute the density profile of fermions in the steady state. In what follows we study the quantities

$$\begin{aligned} N_{0j}(T) &= \langle 2(\hat{n}_j - 1/2) \rangle \\ N_{\text{av}}(T) &= \frac{4}{L} \sum_{j=1..L} \langle (\hat{n}_j - 1/2)^2 \rangle \end{aligned} \quad (9)$$

where the average is taken with respect to the steady state reached under a Floquet drive starting from $|\psi_{\text{init}}\rangle$. In terms of the Floquet eigenfunctions $|\psi_m\rangle$ and the overlap coefficients c_m^{init} (Eq. 8) these can be expressed as

$$\begin{aligned} N_{0j}(T) &= \sum_m |c_m^{\text{init}}|^2 \langle \psi_m | 2(\hat{n}_j - 1/2) | \psi_m \rangle \quad (10) \\ N_{\text{av}}(T) &= \frac{4}{L} \sum_{j=1..L} \left(\sum_m |c_m^{\text{init}}|^2 \langle \psi_m | (\hat{n}_j - 1/2) | \psi_m \rangle \right)^2 \end{aligned}$$

We note that for the initial state $|\langle\psi_{\text{init}}|\hat{2}(\hat{n}_j - 1/2)|\psi_{\text{init}}\rangle|^2 = 0$ and $|\langle\psi_{\text{init}}|\hat{2}(\hat{n}_j - 1/2)|\psi_{\text{init}}\rangle|^2 = 1$ while for free fermions, the ground state with $\mathcal{J}_0 \gg V_0$, $\langle 2(\hat{n}_j - 1/2) \rangle = 0$. Thus $N_{\text{av}}(T)$ provides a measure of degree of delocalization of the driven chain. A similar reasoning shows that $N_{0j} \rightarrow 0$ for all sites in the delocalized regime and $N_{0j} = 1[-1]$ for $j < [>]L/2$ in the localized regime; in contrast, in the presence of a mobility edge, N_{0j} takes values between 0 and 1 at different sites.

A plot of N_{0j} as a function of site index j/L and drive frequency ω_D for the steady state is shown in the left panel of Fig. 7. The density profile is seen to stay close to that of the initial state confirming localization at high drive frequency. In contrast, at low drive frequencies, it approaches zero as expected for the delocalized regime with $\mathcal{J}_0 \gg V_0$. In between, N_{0j} indicates intermediate behavior showing signature of partial transport such that $0 < |N_{0j}| < 1$. The distribution of N_{0j} is much more spread out in the case where the mobility edge separates delocalized and multifractal (as opposed to localized) states as can be clearly seen from the bottom panels of Fig. 7. Thus we find that fermion number distribution in the steady state may provide a signature of presence of the multifractal state in the driven AA model. A plot of $N_{\text{av}}(T)$ as a function of ω_D , shown in the top right panel of Fig. 7, also confirms this behavior. We note that an increased value of $N_{\text{av}}(T)$ (between 0 for perfectly delocalized states and 1 perfectly localized states) for $0.15\pi < \hbar\omega_D/\mathcal{J}_0 < 0.25\pi$ is a signature of presence of both localized (or multifractal) and delocalized states in the Floquet spectrum and hence provides an indication

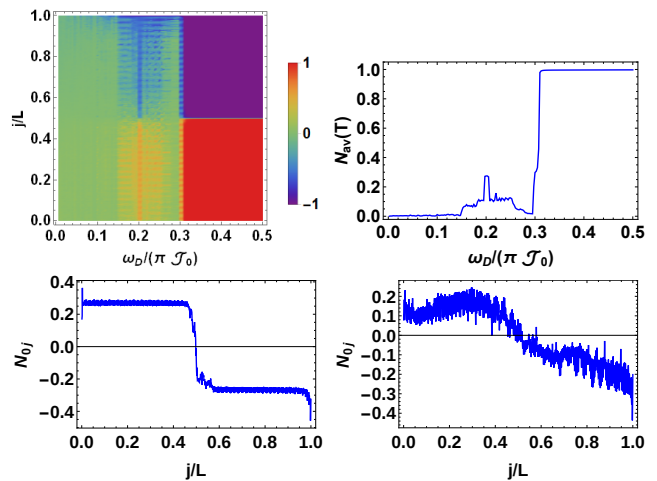


FIG. 7: Top Left Panel: Plot of N_0 as a function of j/L and $\omega_D/(\pi\mathcal{J}_0)$ showing fermion density profile at all sites of the chain in the steady state as a function of $\omega_D/(\pi\mathcal{J}_0)$. Top Right Panel: Plot of $N_{\text{av}}(T)$ as a function of $\omega_D/(\pi\mathcal{J}_0)$ in the steady state showing $0 \leq N_{\text{av}}(T) \leq 1$ for $0.15 \leq \omega_D/(\pi\mathcal{J}_0) \leq 0.25$. Bottom Panels: Plot of N_{0j} as a function of j/L for $\omega_D/(\pi\mathcal{J}_0) = 0.2$ (left) where the mobility edge separates the delocalized and localized states and $\omega_D/(\pi\mathcal{J}_0) = 0.175$ (right) where it separates the delocalized and multifractal states. All other parameters are same as in Fig. 1. See text for details.

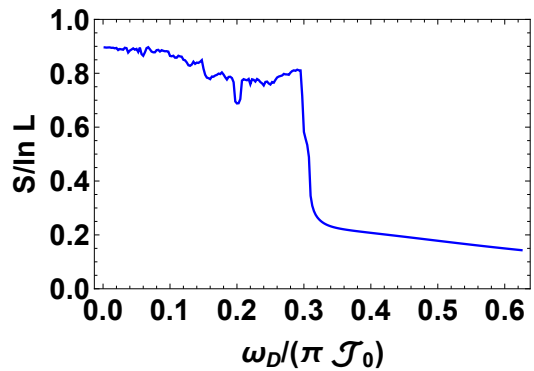


FIG. 8: Plot of the mean Shannon entropy $S/\ln L$ as a function of $\omega_D/(\pi\mathcal{J}_0)$. All other parameters are same as in Fig. 1. See text for details.

of the presence of mobility edge in the spectrum. Moreover, the value of $N_{\text{av}}(T)$ seems to be larger in a narrow frequency range around $\hbar\omega_D/\mathcal{J}_0 = 0.2\pi$ where the mobility edge separates delocalized and localized states. Thus our results show that the local fermion density in the steady state starting from a domain-wall initial condition in these chains may serve as a detector of mobility edge in the Floquet spectrum.

Next, we compute the Shannon entropy of the driven chain. This is defined in terms of the overlap coefficients obtained by computing overlap of the single-particle Floquet eigenstates $|\psi_m\rangle$ with the eigenstates of $H_p = H_F(T=0)$ $|j\rangle$: $\psi_m(j) = \langle j|\psi_m\rangle$. The Floquet eigenstates can be written as $|\psi_m\rangle = \sum_j \psi_m(j)|j\rangle$. The

Shannon entropy of the m^{th} Floquet eigenstate is then given by²⁹

$$S_m = - \sum_j |\psi_m(j)|^2 \ln |\psi_m(j)|^2, \quad S = \frac{1}{L} \sum_m S_m \quad (11)$$

where S is the mean entropy. We note that for high frequency when $H_F \simeq H_p$, $\psi_m(j) \simeq \delta_{mj}$ leading to $S_m \simeq 0$ for $\hbar\omega_D/\mathcal{J}_0 \gg 1$ by construction. Since eigenfunctions of H_p are localized this means that $S \rightarrow 0$ for localized states. In contrast for $\hbar\omega_D/\mathcal{J}_0 \ll 1$ when all Floquet eigenstates are delocalized, $\psi_m(j) \simeq 1/\sqrt{L}$ for all m leading to maximum entropy of $S \simeq \ln L$. A plot of $S/\ln L$ as a function of the drive frequency, shown in Fig. 8, indicates this change. We find that the localization-delocalization transition is marked by a sharp rise in S around $\omega_D = \omega_c = 0.3\pi\mathcal{J}_0/\hbar$. The appearance of the mobility edge just below the transition leads to $S/\ln L \leq 1$; this value would have been closer to unity if all the Floquet eigenstates would be delocalized for $\omega_D \leq \omega_c$. We note that S shows a narrow dip around $\hbar\omega_D/\mathcal{J}_0 = 0.2\pi$. This can be understood to be due to the fact that around this frequency the mobility edge separates localized, rather than multifractal, states from the delocalized ones; the presence of these localized states in the spectrum leads to a lower value of S .

Finally we compute the survival probability which is defined as the probability of finding a fermion, initially localized at a given site, within a neighborhood of length R around that site after n drive cycles. This is given by

$$F_n(R) = \sum_{j=j_0-R/2}^{j_0+R/2} |\psi_n(j)|^2$$

$$\psi_n(j) = U(nT, 0)\psi_{\text{init}}(j) \quad (12)$$

where j denotes lattice sites, we shall consider the initial wavefunction to be localized at the center of the chain ($j_0 = L/2$) for the rest of this section. The limiting values of $F_n(R)$ can be easily deduced. For example, if the wavefunction remains localized $F_n(R) \simeq 1$ for all R and n ; in contrast if the drive leads to delocalization, $F_n(R)$ should linearly increase with R for large n . In the presence of a mobility edge separating delocalized and multifractal states, $F_n(R)$ should again increase with R , but with a sublinear growth for large n . Moreover, the steady state value of $F_n(R)$ can be obtained in terms of Floquet eigenfunctions as

$$F_s(R) = \sum_{j=j_0-R/2}^{j_0+R/2} \sum_m |\psi_m(j)|^2 \quad (13)$$

and is therefore controlled by the coefficients $\psi_m(j)$.

A plot of $F_s(R = L/2)$ as a function of the drive frequency ω_D is shown in the left panel of Fig. 9. We find that $F_s(L/2)$ shows a sharp dip at the localization-delocalization transition. Below the transition, the decay

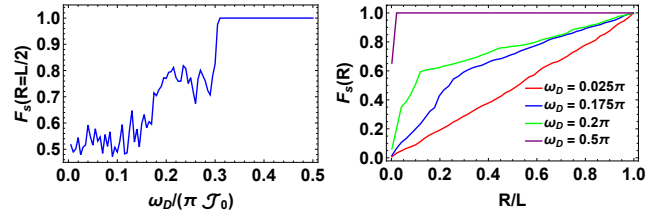


FIG. 9: Left Panel: Plot of the survival probability $F_s(L/2)$ as a function of $\omega_D/(\pi\mathcal{J}_0)$. Right panel: Plot of $F_s(R)$ as a function of R for several representative value of $\omega_D/(\pi\mathcal{J}_0)$. All other parameters are same as in Fig. 1. See text for details.

of $F_s(L/2)$ is gradual and non-monotonic; this seems to be a direct consequence of the presence of the mobility edge. The right panel of Fig. 9 shows the R dependence of $F_s(R)$ for several representative drive frequencies. We find that at high drive frequencies $\hbar\omega_D/\mathcal{J}_0 = 0.5\pi$, the system remains localized leading to $F_s \simeq 1$ for almost all R ; in contrast it linearly decreases to zero as R is decreased in the low frequency limit $\hbar\omega_D/\mathcal{J}_0 = 0.025\pi$. In between, in the regime where the mobility edge separates delocalized states from multifractal or localized states in the Floquet eigenspectrum, we find sublinear decay of $F_s(R)$ as a function of R ; this decay is faster if states with quasienergies above the mobility edge are localized ($\hbar\omega_D/\mathcal{J}_0 = 0.2\pi$). Thus $F_s(R)$ distinguishes between mobility edge separating delocalized states with multifractal or localized states.

Finally, we study the V_0 dependence of our results. In particular we concentrate on obtaining an estimate of the range of V_0/\mathcal{J}_0 over which the multifractal states exist. To this end, we plot the mean Shannon entropy of the Floquet eigenstates as a function of V_0 and ω_D . This plot, shown in the left panel of Fig. 10, indicates that a mobility edge separating delocalized and multifractal states (indicated by blue in the plot) are present of over a range of frequency whose width tend to be maximal around $V_0 \ll \mathcal{J}_0$. For $V_0 \geq \mathcal{J}_0$, the Floquet states are either all localized (red region) or display a mobility edge separating delocalized and localized states (green regions). For $V_0, \hbar\omega_D \ll \mathcal{J}_0$, the Floquet states are all delocalized (violet regions). The right panel shows a plot of $S/\ln L$ as a function of V_0 for $\hbar\omega_D/\mathcal{J}_0 = 0.22\pi$. The plot shows indication of a mobility edge separating delocalized and localized states for $0.8 \leq V_0/\mathcal{J}_0 \leq 0.2$; in contrast, the mobility edge separates delocalized and multifractal states for $V_0/\mathcal{J}_0 \leq 0.2$. Thus our results show that the multifractal states are indeed present in the Floquet spectrum for a wide region in the $(V_0/\mathcal{J}_0, \hbar\omega_D/\mathcal{J}_0)$ plane.

B. Sinusoidal Protocol

In this section, we study the properties of AA model in the presence of a continuous drive. Such a drive is

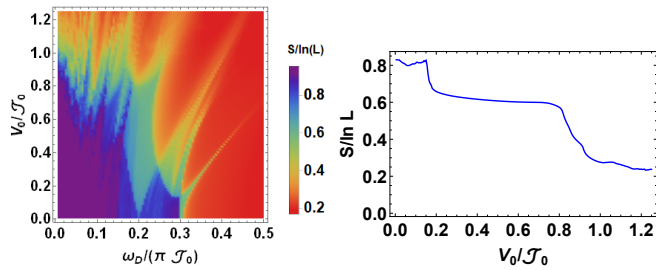


FIG. 10: Left panel: Distribution of $S/\ln L$ as a function of the Aubrey Andre Strength V_0/\mathcal{J}_0 and the drive frequency $\omega_D/(\pi\mathcal{J}_0)$. The regions with all localized states are indicated by red, delocalized states by violet. The blue regions denote mixture of delocalized and multifractal states and green mixture of delocalized and localized states. Right Panel: Plot of $S/\ln L$ as a function of V_0/\mathcal{J}_0 for $\hbar\omega_D/(\pi\mathcal{J}_0) = 0.22$. All other parameters are same as in Fig. 1.

implemented by choosing

$$\mathcal{J}(t) = \mathcal{J}_0 \cos \omega_D t \quad (14)$$

A numerical study of the AA model in the presence of such a continuous drive involves decomposition of the evolution operator into N Trotter steps such $H(t)$ does not change significantly in the interval t_j and $t_j + T/N$ for any time instant t_j . One can define the eigenvalues and eigenfunctions of the instantaneous Hamiltonian $H_j = H[t_j + T/(2N)]$ as ϵ_n^j and $|\psi_n^j\rangle$; these are obtained numerically by exact diagonalization of H_j on a lattice of size L . One can then construct the evolution operator as

$$U(T, 0) = \prod_{j=1}^N \sum_n e^{-i\epsilon_n^j T/N} |\psi_n^j\rangle \langle \psi_n^j| \quad (15)$$

We note this procedure requires numerical diagonalization of N instantaneous Hamiltonians; this make numerical study of continuous protocols significantly more costly compared to their discrete counterparts. Having constructed $U(T, 0)$, we diagnosable it numerically to obtain the eigenvalues and eigenfunctions of the Floquet Hamiltonian as outlined in Sec. II A.

The results obtained from this procedure is shown in Fig 11. We find that the all properties of the driven systems, such as the presence of a mobility edge in the Floquet spectrum, the presence of multifractal Floquet eigenstates, their signature in transport, and the presence of the CAT states remain qualitatively similar; however, the position of the localization-delocalization transition shows a significant change. From the plot of I_m as a function of ω_D and m in the top left panel of Fig. 11, we find that the transition shifts to $\hbar\omega_D/\mathcal{J}_0 \simeq 0.25\pi$; the mobility edge exists over narrower regions (one near $0.16\pi \leq \hbar\omega_D/\mathcal{J}_0 \leq 0.18\pi$ and another near $0.2\pi \leq \hbar\omega_D/\mathcal{J}_0 \leq 0.25\pi$) as can be seen from the plot of τ_2 as a function of m and ω_D in the top right panel. A plot of D_q shown in the middle left panel confirms the presence of multifractal states in these regions. In the

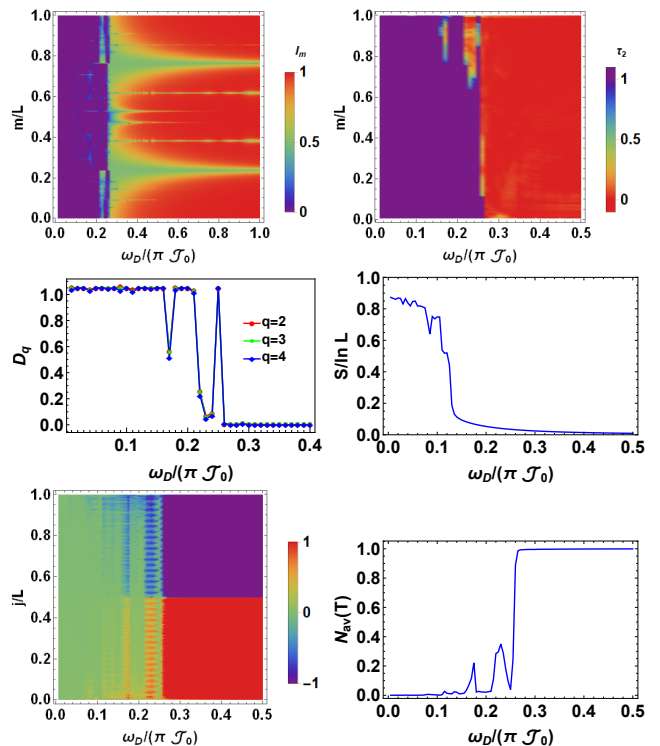


FIG. 11: Top Left Panel: Plot of I_m as a function of m/L and $\omega_D/(\pi\mathcal{J}_0)$. Top Right Panel: Plot of τ_2 as a function of m/L and $\omega_D/(\pi\mathcal{J}_0)$. Middle Left Panel: Plot of D_q as a function of $\omega_D/(\pi\mathcal{J}_0)$ for $m/L = 0.75$. Middle Right Panel: A plot of S as a function of $\omega_D/(\pi\mathcal{J}_0)$ showing the signature of localization-delocalization transition at $\hbar\omega_D/(\pi\mathcal{J}_0) \simeq 0.25$. Bottom left Panel: Plot of N_{0j} as a function of j/L and $\omega_D/(\pi\mathcal{J}_0)$ showing fermion density profile at all sites of the chain in the steady state as a function of $\omega_D/(\pi\mathcal{J}_0)$. Bottom right Panel: Plot of N_{av} as a function of $\omega_D/(\pi\mathcal{J}_0)$. The system sizes used to calculate τ_2 and D_q is $L = 200 \sim 1600$ in steps of 200. The other plots are presented at $L = 1024$. Here $V_0/\mathcal{J}_0 = 0.025$, all other parameters are same as in Fig. 1. See text for details.

middle right panel, we show the plot of the mean Shannon entropy S as a function of ω_D . We find that S also bears the signature of the localization-delocalization transition. The bottom panels show steady state distribution of particles in this system starting from the domain wall state. The bottom left panel shows the distribution of N_{0j} over lattice sites (scaled by system size (L)) as a function of the drive frequency. The plot demonstrates the non-monotonic behavior of N_{0j} as a function of ω_D just below the transition. Finally the bottom right panel shows a plot of N_{av} as a function of ω_D in the steady state; we find that it displays signature of the localization-delocalization transition around $\hbar\omega_D/\mathcal{J}_0 = 0.25\pi$ and also shows peaks at intermediate frequency where the mobility edge appears in the spectrum. The height of these peaks are less than unity; this is a consequence of the fact that the entire spectrum is not localized at these frequencies.

Finally, we plot the mean Shannon entropy $S/\ln L$ as

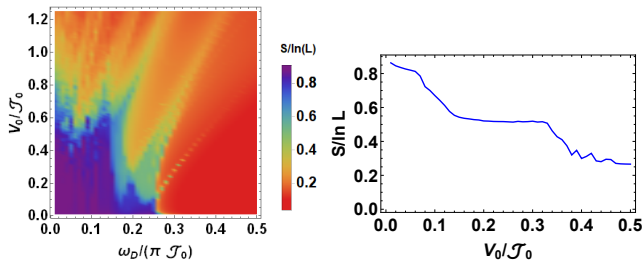


FIG. 12: Left: Plot of $S/\ln L$ as a function of V_0/\mathcal{J}_0 and $\omega_D/(\pi\mathcal{J}_0)$ for the sinusoidal protocol with $L = 610$. Right: Plot of $S/\ln L$ as a function of V_0/\mathcal{J}_0 for a cut taken at $\hbar\omega_D/(\pi\mathcal{J}_0) = 0.22$. All other parameters are same as in Fig. 1.

a function of V_0 and ω_D . We find that for the sinusoidal protocol the presence of multifractal states occurs in a reduced area of parameter space compared to that for square pulse protocol studied earlier. Moreover, we get localized states at a lower frequency as compared to square pulse protocol for the same value of V_0 . From both the graphs we observe that as we increase V_0 the frequency at which all states becomes localized decreases. This expected since the off-diagonal hopping terms becomes small compared to the diagonal AA potential term leading to dynamical localization.

Our results therefore indicate that the localization-delocalization transition in these systems along with the presence of the CAT and multifractal state exists for both discrete and continuous protocols. However, the range of ω_D for which the multifractal states exists is significantly reduced in the latter case.

III. FLOQUET PERTURBATION THEORY

In this section, we aim to obtain an analytic, albeit perturbative, understanding of several features of the driven AA model found via exact numerics using FPT which is known to provide accurate results in the large drive amplitude limit^{17,21,22}. The square pulse protocol will be treated in Sec. III A while the continuous drive protocol will be addressed in Sec. III B.

A. FPT for square pulse protocol

In this section, we shall focus on the square pulse protocol given by Eq. 2 in the large drive amplitude limit $\mathcal{J}_0 \gg V_0$. In this limit, we consider the contribution from H_p to the evolution operator $U(T, 0)$ as perturbation and develop a systematic expansion for U following Refs. 17,21,22. To this end, we first note that the first term in such an expansion is given by U_0 which can be

written as $U_0 = \prod_k U_{0k}$ where

$$\begin{aligned} U_{0k}(t, 0) &= e^{it\mathcal{J}_0 \cos k c_k^\dagger c_k}, \quad t \leq T/2 \\ &= e^{i(T-t)\mathcal{J}_0 \cos k c_k^\dagger c_k}, \quad T/2 \leq t \leq T \end{aligned} \quad (16)$$

Here and in the rest of this section, we have set \hbar to unity. This leads to $U_0(T, 0) = I$ (where I denotes the identity matrix) and $H_{F0} = 0$. The vanishing H_{F0} can be seen to be the consequence of the symmetric nature of the drive protocol.

The first order perturbative correction of U_0 , within FPT, is given by

$$U_1 = -i \int_0^T dt U_0^\dagger(t, 0) H_p U_0(t, 0) \quad (17)$$

To evaluate this, we use the number basis in momentum space, $|k\rangle \equiv |n_k\rangle$, since U_0 is diagonal in this basis. The matrix element of U_1 in this basis is then given by

$$\begin{aligned} \langle k_1 | U_1 | k_2 \rangle &= \frac{4V(k_1 - k_2)}{\mathcal{J}_0 f(k_1, k_2)} \sin[\mathcal{J}_0 f(k_1, k_2)T/4] \\ &\quad \times e^{iT\mathcal{J}_0 f(k_1, k_2)/4} \end{aligned} \quad (18)$$

$$V(k) = V_0 \sum_j \exp[ikj] \cos(2\pi\eta j) = V(-k),$$

$$f(k_1, k_2) = \cos k_2 - \cos k_1 = -f(k_2, k_1)$$

where we have set $\phi = 0$ without loss of generality. This indicates that the Floquet Hamiltonian to first order in perturbation theory is given by^{21,22}

$$\begin{aligned} H_{F1} &= i \sum_{k_1, k_2} \frac{4V(k_1 - k_2)}{\mathcal{J}_0 T f(k_1, k_2)} \sin[\mathcal{J}_0 f(k_1, k_2)T/4] \\ &\quad \times e^{iT\mathcal{J}_0 f(k_1, k_2)/4} c_{k_1}^\dagger c_{k_2} \end{aligned} \quad (19)$$

A similar procedure for $U_2(T, 0)$ yields the relation $U_2(T, 0) = U_1(T, 0)^2/2$ and thus yield $H_{F2} = 0$. The details of this calculation is similar to that carried out in Ref. 17 and is not presented here. In what follows, we shall analyze H_{F1} (Eq. 19) with the aim of obtaining qualitative understanding of the presence of multifractal states in the Floquet spectrum.

A straightforward numerical diagonalization of H_{F1} yields the Floquet eigenstates and eigenvalues. To study the nature of these Floquet eigenstates as a function of drive frequency, we plot the IPR I_m and τ_2 corresponding to these states in Fig. 13. The top left panel of this plot shows the plot of I_m as a function of m/L and ω_D . I_m obtained from the eigenstates of H_{F1} retains all qualitative feature of the Floquet eigenstates obtained from exact numerics. In particular, the plot shows a localization-delocalization transition around $\hbar\omega_D/\mathcal{J}_0 \simeq 0.3\pi$ which is close to the exact value $\hbar\omega_c/\mathcal{J}_0 = 0.3\pi$. Moreover, the spectrum indicates the presence of the CAT states in the spectrum; we have checked that the origin of these state can be tracked back to the flat regions in the Floquet spectrum as can be seen from the top

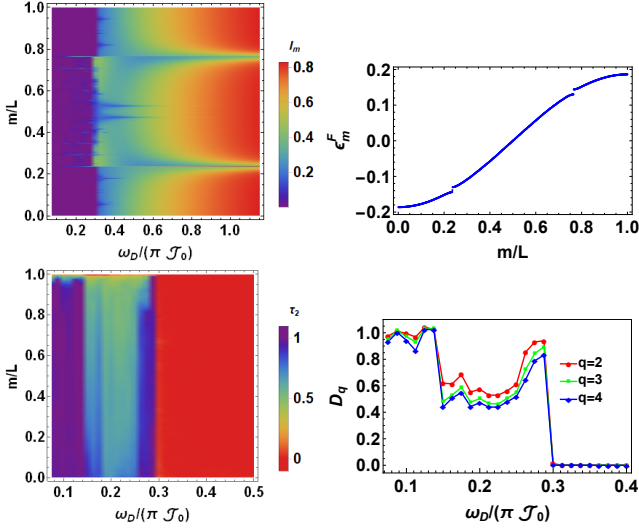


FIG. 13: Top Left Panel: Plot of I_m as a function of m/L and $\omega_D/(\pi\mathcal{J}_0)$. Top Right Panel: Plot of eigenstates ϵ_m^F obtained by diagonalizing H_{F1} as a function of m/L for $\hbar\omega_D/(\pi\mathcal{J}_0) = 1$. Bottom Left Panel: Plot of τ_2 as a function of m/L and $\omega_D/(\pi\mathcal{J}_0)$. Bottom right Panel: Plot of D_q as a function of $\omega_D/(\pi\mathcal{J}_0)$ for $m/L = 0.75$. All other parameters are same as in Fig. 1 and Fig. 5. See text for details.

right panel of Fig. 13. The bottom left panel shows a plot of τ_2 as a function of m/L and ω_D . We find that just below the transition, we find a wide range

of frequency $0.15\pi \leq \hbar\omega_D/\mathcal{J}_0 \leq 0.3\pi$ where we find states with $0 < \tau_2 < 1$ signifying the possibility of existence of multifractal states. However, we note the mobility edge is now restricted to a very narrow region $0.26\pi \leq \hbar\omega_D/\mathcal{J}_0 \leq 0.3\pi$; for $0.15\pi \leq \hbar\omega_D/\mathcal{J}_0 \leq 0.25\pi$ we do not find delocalized states in the spectrum which is contrast with that obtained in exact numerics. The presence of multifractal states in the spectrum of H_{F1} is further confirmed by plotting D_q for $q = 2, 3, 4$ as a function of ω_D for $m/L = 0.75$ in the bottom right panel of Fig. 13; the plot shows clear signature of multifractality for $0.15\pi \leq \hbar\omega_D/\mathcal{J}_0 \leq 0.3\pi$. Our results indicate that H_{F1} constitutes semi-analytic expression of a Floquet Hamiltonian which support multifractal states in its eigenspectrum.

To understand the origin of these multifractal states, we obtain a real space representation of H_{F1} . A Fourier transform of Eq. 19 yields

$$\begin{aligned}
 H_{F1} &= \sum_{j,j'} H_{jj'} c_j^\dagger c_{j'} \\
 H_{jj'} &= \int_{-\pi}^{\pi} \frac{dk_1 dk_2}{2\pi} e^{i(k_1 j - k_2 j')} \frac{4iV(k_1 - k_2)}{\mathcal{J}_0 T f(k_1, k_2)} \\
 &\quad \times \sin[\mathcal{J}_0 f(k_1, k_2) T/4] e^{iT\mathcal{J}_0 f(k_1, k_2)/4} \quad (20)
 \end{aligned}$$

A straightforward calculation outlined in the Appendix leads to an analytic expression for $H_{jj'}$ given by

$$\begin{aligned}
 H_{jj'} &= \frac{i}{2\sqrt{2}} \sum_{w=|j-j'|/2}^{\infty} \frac{(T\mathcal{J}_0)^{2w}}{(2w+1)} \frac{\sqrt{\pi}}{\kappa'(j, j', 2w)} \left[\frac{1}{2^{2w-1}} \binom{2w}{w} V[(j+j')/2] \right. \\
 &\quad \left. + \frac{(-1)^w}{2^{2w-1}} \sum_{z=0}^{w-1} (-1)^z \binom{2w}{z} (V[(w-z) + (j+j')/2] + V[(j+j')/2 - (w-z)]) \right] \quad j - j' = 2n \\
 &= -\frac{1}{2\sqrt{2}} \sum_{w=(|j-j'-1|)/2}^{\infty} \frac{(T\mathcal{J}_0)^{2w+1}}{(2w+2)} \frac{\sqrt{\pi}}{\kappa'(j, j', 2w+1)} \frac{(-1)^w}{4^w} \sum_{z=0}^w (-1)^z \binom{2w+1}{z} \\
 &\quad \times (V[(j+j')/2 - (2w+1-2z)/2] - V[(j+j')/2 + (2w+1-2z)/2]), \quad j - j' = 2n + 1 \quad (21)
 \end{aligned}$$

where n is an integer and the function κ' is given by

$$\begin{aligned}
 \kappa'(m, n, p) &= 1, \quad p = 0 \quad (22) \\
 &= |m-n| \prod_{s=1, s \neq |m-n|/2}^{p/2} [(m-n)^2 - (2s)^2], \quad p = 2k \\
 &= \prod_{s=0, s \neq (|m-n|-1)/2}^{(p-1)/2} [(m-n)^2 - (2s+1)^2], \quad p = 2k+1
 \end{aligned}$$

for integer k . From the expression of $H_{jj'}$ we clearly find that the Floquet Hamiltonian corresponds to a hop-

ping Hamiltonian whose range increases with decreasing drive frequency. At very high frequencies, only the $j = j'$ (on-site) term survives and we get back the Magnus result. As the frequency is decreased, the amplitude of terms for which $j \neq j'$ (hopping terms with range $|j - j'|$) increases. Thus at intermediate frequencies, this corresponds to a Hamiltonian with on-site quasiperiodic term (corresponding to $j = j'$) and intermediate range hopping terms (for both odd and even $|j - j'|$) whose amplitude depends on the drive frequency. It is well known that similar Hamiltonians, for specific range of hopping amplitudes, supports multifractal states in their

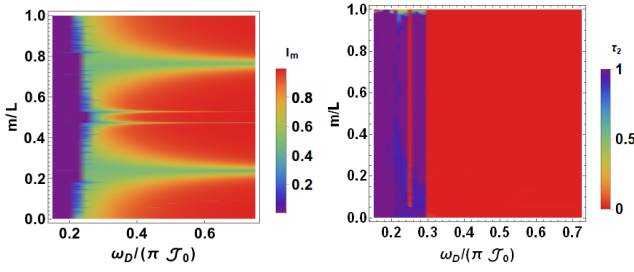


FIG. 14: Left Panel: Plot of I_m as a function of m/L and $\omega_D/(\pi\mathcal{J}_0)$. Right Panel: Plot of τ_2 as a function of m/L and $\omega_D/(\pi\mathcal{J}_0)$. All other parameters are same as in Fig. 1 and Fig. 5. See text for details.

spectrum³. We point out that here the drive frequency may be used to engineer these amplitudes. Our result thus constitutes an example of analytic form of a Floquet Hamiltonian which supports multifractal states.

B. FPT for continuous protocol

For the continuous protocol, we choose $\mathcal{J}(t) = \mathcal{J}_0 \cos(\omega_D t)$ so that for $\mathcal{J}_0 \gg V_0$, U_0 is given by

$$U_0(t, 0) = \exp \left[-\frac{i\mathcal{J}}{\omega_D} \sin(\omega_D t) \sum_n c_k^\dagger c_k \right] \quad (23)$$

where we have set $\hbar = 1$. This leads to $U_0(T, 0) = I$ and $H_{F0} = 0$. We note that the eigenbasis for U_0 is still given by $|k\rangle \equiv |n_k\rangle$

The perturbative contribution to the first order term in the Floquet Hamiltonian is then by Eq. 17 with $U_0(t, 0)$ given by Eq. 23. A straightforward calculation shows that the matrix elements of U_1

$$\langle k_1 | U_1(T, 0) | k_2 \rangle = -iTV(k_1 - k_2)J_0(x_{12}) \quad (24)$$

where J_0 denotes Bessel functions and $x_{12} = \mathcal{J}_0 f(k_1, k_2)/\omega_D$. Using this, we find that the first order Floquet Hamiltonian is given by

$$H_{F1} = \sum_{k_1, k_2} V(k_1 - k_2) J_0(x_{12}) c_{k_1}^\dagger c_{k_2} \quad (25)$$

We note that for $\omega_D \rightarrow \infty$, $J_0 \rightarrow 1$ and $H_{F1} \rightarrow H_p$ which reproduces the Magnus results. The second order terms can be computed in an analogous fashion. The computation procedure is same as charted out in Ref. 22 and yields

$$H_{2F} = \sum_{k_1, k_2, k_3, k_4} \sum_{n=0}^{\infty} \frac{V(k_1 - k_2)V(k_3 - k_4)}{(2n+1)\omega_D} [J_0(x_{12})J_{2n+1}(x_{34}) - J_0(x_{34})J_{2n+1}(x_{12})] c_{k_1}^\dagger c_{k_2} c_{k_3}^\dagger c_{k_4}. \quad (26)$$

We note that $H_{2F} \rightarrow 0$ as $\omega_D \rightarrow \infty$ which is consistent with the Magnus expansion results which yields a vanishing second order contribution to H_F .

Next, we obtain the Floquet eigenstates and corresponding quasienergies via numerical diagonalization of $H_F = H_{1F} + H_{2F}$. The results are shown in Fig. 14. Again, qualitative features like the presence of CAT states, mobility edge and multifractal states are all captured by the perturbative H_F obtained from FPT. The FPT results also show a significant reduction in the range of drive frequencies ω_D that give rise to multifractal

states consistent with the exact numerics for the sinusoidal protocol.

Finally we obtain a representation of H_F in real space following an analysis which is identical to that carried out in the previous section for the square-pulse protocol. For this purpose, we consider H_{F1} and obtain its analytic form in real space. The details of the calculation in charted out in the appendix. This yields $H_{1F} = \sum_{jj'} H_{jj'} c_j^\dagger c_{j'}$ where $H_{jj'} = 0$ for $|j - j'| = 2m + 1$. For $|j - j'| = 2m$, it is given by

$$\begin{aligned}
H_{jj'} = & \sum_{p=(j-j')/2}^{\infty} \frac{(-1)^p 2(2p)! (\mathcal{J}_0 T / (2\pi))^{2p} \sqrt{\pi}}{p! 2^{p-1} 4\Gamma(p+1) \kappa(j, j', p)} \left[\binom{p}{p/2} V((j+j')/2) \right. \\
& \left. + (-1)^{p/2} \sum_{z=0}^{p/2-1} (-1)^z \binom{p}{z} (V[(p/2-z) + (j+j')/2] + V[(j+j')/2 - (p/2-z)]) \right] \\
\kappa(m, n, p) = & 1, \quad \text{for } p=0, \quad \kappa(m, n, p) = (m-n) \prod_{s=1, s \neq (m-n)/2}^p [(m-n)^2 - (2s)^2], \quad \text{otherwise} \quad (27)
\end{aligned}$$

We note that similar to the square pulse protocol, we get a real-space Floquet whose range increases with decreasing frequency. The high-frequency limit leads to a completely local Hamiltonian consistent with the Magnus result. However, for the continuous drive protocol discussed in this subsection, H_{1F} only induces next-nearest neighbor couplings. The coupling between odd and higher neighboring sites which differ by an odd number of lattice sites is induced by H_{2F} . We do not compute this terms here but merely observe that their contribution would be smaller by at least a factor of V_0/ω_D . The difference in coupling strength between sites differing by odd and even number of lattice sites also explains the reason for the structure of the CAT states. We find that they are distributed between a site and its next-nearest neighbor (rather than the expected nearest one). This is clearly a consequence of having larger $H_{jj'}$ between the next-nearest neighbor sites compared to the nearest ones.

IV. DISCUSSION

In this work, we have charted out the phase diagram of the driven AA model using both square pulse and sinusoidal drive protocols. Our numerical studies, carried out using exact diagonalization of the fermionic system, reveals the presence of localization-delocalization transition in this system occurring at a critical drive frequency ω_c . Moreover, below ω_c , for a range of drive frequencies, we find the existence of a mobility edge which separates delocalized Floquet eigenstates with quasienergies below the edge from localized or multifractal eigenstates above it. Our analysis shows the presence of multifractal states in the Floquet eigenspectrum over a wide range of drive frequencies. We show that the presence of the mobility edge leaves its imprint on the transport of the system and on survival probability and Shannon entropy of the driven fermions. Moreover, the fermion transport starting from a domain wall state where all the fermions are localized to the left-half of the chain can discern the presence of multifractal states in the Floquet eigenspectrum. We note that the non-driven AA model does not support mobility edge or multifractal states in its spectrum; thus our results constitute dynamical signatures which have

no analog in the non-driven model.

The numerical results that we find can be semi-analytically understood within FPT. Our results regarding this constitutes derivation of semi-analytic, albeit perturbative, Floquet Hamiltonians for both square pulse and sinusoidal drive protocols. We show that these perturbative, semi-analytic Hamiltonians reproduce the localization-delocalization transition obtained numerically; moreover, they support CAT and multifractal states in their eigenspectrum. The reason for the presence of such states can be understood by obtaining real-space representation of these Hamiltonians. In real-space, these Floquet Hamiltonians contain on-site quasiperiodic terms along with hopping terms which connects between fermions at different sites. We find that the range of these latter class of terms increase with decreasing drive frequency. Consequently, these Floquet Hamiltonians belong to a class of Hamiltonians with Aubrey-André interactions and quasi-long range hopping terms. It was shown in Ref. 3 that these Hamiltonian support multifractal states.

Our results indicate that the signature of the localization-delocalization transition can be obtained by studying fermionic transport. This allows us to suggest realistic experiment which can test our theory. We suggest realization of the Aubrey-André potential in an optical lattice as done recently in Ref. 6. The drive of the hopping term may be induced by tuning the laser strength creating the optical lattice using either of the periodic protocols discussed. In addition, one can start from a configuration where the fermions in the lattice are confined to the left-half of the chain. Our prediction is that there will be critical drive frequency ω_c below which the system will eventually delocalize. This will be reflected in a sharp drop in the value of N_{av}^2 as sketched in Fig. 7. Moreover, for a range of frequencies below ω_c , N_{av}^2 will remain between its values for localized ($N_{av}^2 = 1$) and delocalized ($N_{av}^2 = 0$) states signifying the presence of the mobility edge.

In conclusion, we have studied the driven Aubrey-André model and showed the presence of a drive-induced localization-delocalization transition. Our results indicate the presence of mobility edge and multifractal states in the Floquet eigenstates; their existence can be seen

from analytic, perturbative form of H_F which we derive using a Floquet perturbation theory which represents a resummation of an infinite class of terms in the Magnus expansion. We show that the presence of this mobility edge is reflected in fermionic transport and suggest experiments which can test our theory.

Acknowledgments

The authors acknowledges related discussions at ICTS, Bengaluru during the program Thermalization, Many body localization and Hydrodynamics (Code: ICTS/hydrodynamics2019/11). The work of A.S. is partly supported through the Max Planck Partner Group program between the Indian Association for the Cultivation of Science (Kolkata) and the Max Planck Institute for the Physics of Complex Systems (Dresden).

Appendix A: Real space representation of H_F

1. Square pulse

We start from Eq. 20 from the main text,

$$\begin{aligned} H_{F1} &= \sum_{j,j'} H_{jj'} c_j^\dagger c_{j'} \\ H_{jj'} &= \int_{-\pi}^{\pi} \frac{dk_1 dk_2}{\pi} e^{i(k_1 j - k_2 j')} \frac{4iV(k_1 - k_2)}{\mathcal{J}_0 T f(k_1, k_2)} \\ &\quad \times \sin[\mathcal{J}_0 f(k_1, k_2) T/4] e^{iT\mathcal{J}_0 f(k_1, k_2)/4} \end{aligned} \quad (\text{A1})$$

We shift to the center of momentum coordinates, $q = \frac{k_1 - k_2}{2}$ and $r = \frac{k_1 + k_2}{2}$ where $dqdr = \frac{1}{2} dk_1 dk_2$ and write

$$\begin{aligned} H_{jj'} &= \frac{1}{2\pi} \int_{-\pi}^{\pi} \int_{-\pi}^{\pi} dqdr e^{i[q(j+j') + r(j-j')]} \frac{4iV(2q)}{\mathcal{J}_0 T g(q, r)} \\ &\quad \times \sin[\mathcal{J}_0 g(q, r) T/4] e^{iT\mathcal{J}_0 g(q, r)/4} \end{aligned} \quad (\text{A2})$$

Now expanding the oscillatory part, we write

$$\sin[\mathcal{J}_0 g(q, r) T/4] e^{iT\mathcal{J}_0 g(q, r)/4} = \frac{T}{4} \sum_{p=0}^{\infty} \frac{(iT\mathcal{J}_0 g(q, r)/2)^p}{(p+1)!} \quad (\text{A3})$$

Hence Eq. A2 can be written as,

$$\begin{aligned} H_{jj'} &= \frac{1}{2\pi} \sum_{p=0}^{\infty} \frac{(iT\mathcal{J}_0/2)^p}{(p+1)!} \int_{-\pi}^{\pi} \int_{-\pi}^{\pi} dqdr \\ &\quad \times e^{i[q(j+j') + r(j-j')]} iV(2q) (2 \sin q \sin r)^p \end{aligned} \quad (\text{A4})$$

The next task is to perform the integrals. Performing the integral over r first, we get

$$\begin{aligned} H_{jj'} &= \frac{1}{2\pi} \sum_{p=0}^{\infty} \frac{(iT\mathcal{J}_0/2)^p}{(p+1)!} \int_{-\pi}^{\pi} dq e^{iq(j+j')} \\ &\quad \times iV(2q) (\sin q)^p \frac{2^{p+1} p! (-i)^p \sin[(j-j')\pi]}{\kappa(j, j', p)} \end{aligned} \quad (\text{A5})$$

where

$$\begin{aligned} \kappa(j, j', p) &= (j-j') \prod_{s=1}^{p/2} [(j-j')^2 - (2s)^2], \quad p = 2k \\ &= \prod_{s=0}^{(p-1)/2} [(j-j')^2 - (2s+1)^2], \quad p = 2k+1 \end{aligned} \quad (\text{A6})$$

for any integer k . It is to be noted that only when $s = |j-j'|/2$ for p even and $s = (|j-j'| - 1)/2$ for p odd, the integrals give a finite contribution. Hence the summation over p must start from $p = |j-j'|$. This gives,

$$\begin{aligned} H_{jj'} &= \frac{i}{2\pi} \sum_{p=|j-j'|}^{\infty} \frac{(iT\mathcal{J}_0/2)^p}{(p+1)!} \int_{-\pi}^{\pi} dq e^{iq(j+j')} \\ &\quad \times V(2q) (\sin q)^p \frac{2^{p+1} p! (-i)^p \pi}{\kappa'(j, j', p)} \end{aligned} \quad (\text{A7})$$

where ,

$$\begin{aligned} \kappa'(j, j', p) &= 1, \quad p=0 \\ &= |j-j'| \prod_{s=1, s \neq |j-j'|/2}^{p/2} [(j-j')^2 - (2s)^2], \quad p = 2k \\ &= \prod_{s=0, s \neq (|j-j'| - 1)/2}^{(p-1)/2} [(j-j')^2 - (2s+1)^2], \quad p = 2k+1 \end{aligned} \quad (\text{A8})$$

Next, we perform the integral over q using standard trigonometric identities. First one should separate out the even and odd parts of the integral, and note that when $j-j'$ is even, p necessarily is always even as the rest of the terms integrate to 0 and similarly for $j-j'$ odd. Hence for $j-j'$ even, assuming $p = 2w$, we get

$$H_{jj'} = \frac{i}{2\pi} \sum_{w=|j-j'|/2}^{\infty} \frac{(T\mathcal{J}_0)^{2w}}{(2w+1)} \frac{\pi}{\kappa'(j, j', 2w)} \int_{-\pi}^{\pi} dq \cos[q(j+j')] V(2q) \left[\frac{1}{2^{2w}} \binom{2w}{w} + \frac{(-1)^w}{2^{2w-1}} \sum_{z=0}^{w-1} (-1)^z \binom{2w}{z} \cos[2(w-z)q] \right] \quad (\text{A9})$$

For odd $j - j'$, we consider $p = 2w + 1$ and obtain

$$H_{jj'} = -\frac{1}{2\pi} \sum_{w=(|j-j'|-1)/2}^{\infty} \frac{(T\mathcal{J}_0)^{2w+1}}{(2w+2)} \frac{\pi}{\kappa'(j, j', 2w+1)} \int_{-\pi}^{\pi} dq \sin[q(j+j')] V(2q) \times \frac{(-1)^w}{4^w} \sum_{z=0}^w (-1)^z \binom{2w+1}{z} \sin[(2w+1-2z)q] \quad (\text{A10})$$

Using the inverse Fourier transform $\frac{1}{\sqrt{2\pi}} \int_{-\pi}^{\pi} V(2q) e^{i2qx} = V(x)$ and integrating over q , we get Eq. 21 of the main text.

2. Sinusoidal pulse

For this drive protocol we start from

$$H_{jj'} = \frac{1}{2\pi} \int_{-\pi}^{\pi} \int_{-\pi}^{\pi} dk_1 dk_2 e^{i[k_1 j - k_2 j']} V(k_1 - k_2) \times J_0(\mathcal{J}_0 f(k_1, k_2)/\omega_D) \quad (\text{A11})$$

As in the case of square protocol, we switch to relative and center of mass momenta and obtain

$$H_{jj'} = \frac{1}{4\pi} \int_{-\pi}^{\pi} \int_{-\pi}^{\pi} dq dr e^{i[q(j+j') + r(j-j')]} V(2q) \times J_0(\mathcal{J}_0 g(q, r)/\omega_D) \quad (\text{A12})$$

where $g(q, r) = -2(\sin q \sin r)$. Next, we use the expansion of $J_0(x)$,

$$J_0(x) = \sum_{p=0}^{\infty} \frac{(-1)^p}{p! \Gamma(p+1)} (x/2)^{2p} \quad (\text{A13})$$

Substituting Eq. A13 in Eq. A12 we find,

$$H_{jj'} = \sum_{p=0}^{\infty} \frac{1}{4\pi} \int_{-\pi}^{\pi} \int_{-\pi}^{\pi} dq dr e^{i[q(j+j') + r(j-j')]} V(2q) \times \frac{(-1)^p}{p! \Gamma(p+1)} (\mathcal{J}_0 \sin q \sin r / \omega_D)^{2p} \quad (\text{A14})$$

Integrating over r we get,

$$H_{mn} = -\sum_{p=0}^{\infty} \frac{1}{4\pi} \int_{-\pi}^{\pi} dq e^{i[q(j+j')]} V(2q) \times (\mathcal{J}_0 \sin q / \omega_D)^{2p} \frac{(-1)^{p2} (2p)! \sin[(j-j')\pi]}{p! \Gamma(p+1) \kappa(j, j', p)} \quad (\text{A15})$$

where,

$$\kappa(j, j', p) = |j - j'| \prod_{s=1}^p [(j - j')^2 - (2s)^2],$$

And noting that the summation can only start from $p = (m - n)/2$ we write,

$$H_{jj'} = -\sum_{p=|j-j'|/2, |j-j'| \text{ even}}^{\infty} \frac{1}{4\pi} \int_{-\pi}^{\pi} dq e^{i[q(j+j')]} V(2q) \times (\mathcal{J}_0 T \sin q / (2\pi))^{2p} \frac{(-1)^{p2} (2p)! \pi}{p! \Gamma(p+1) \kappa'(j, j', p)} \quad (\text{A16})$$

where ,

$$\begin{aligned} \kappa'(j, j', p) &= 1, \quad p=0 \\ &= |j - j'| \prod_{s=1, s \neq (j-j')/2}^p [(j - j')^2 - (2s)^2] \\ &\text{otherwise} \end{aligned} \quad (\text{A17})$$

and we have replaced ω_D by $2\pi/T$. One can immediately see if $|j - j'|$ is odd then no term contributes and $H_{jj'} = 0$. Then one can integrate over q as well to get Eq. 27 of the main text. The expressions of the second order term in H_F is quite complicated and we have not analyzed their form in position space. However, we note that these terms are of the form $\sim \sum_{n=0}^{\infty} [J_{2n+1}(x) J_0(y) - J_0(x) J_{2n+1}(y)] / (2n+1)$. Thus from the expansion of $J_n(x)$, it can be seen that these terms would actually give rise to odd powers of $\sin q$. This means that here the terms of $H_{jj'}$ where $j - j'$ odd will be non-zero. The consequence of this is discussed in the main text.

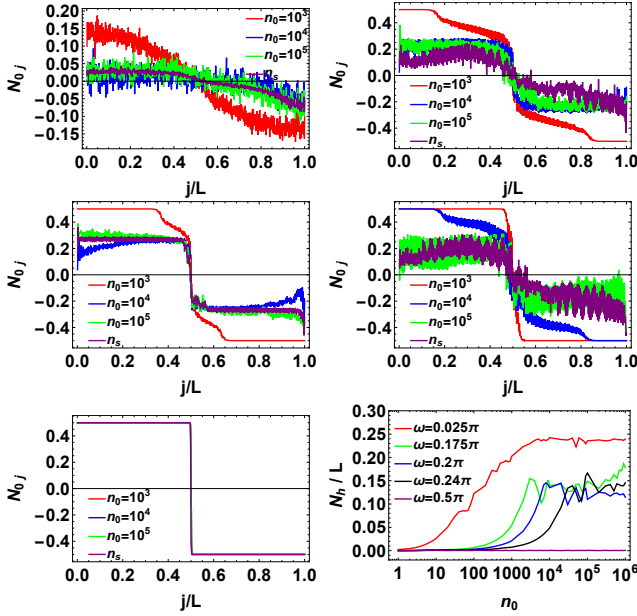


FIG. 15: Top Left Panel: Plot of N_{0j} as a function of j/L for $\omega_D/(\pi\mathcal{J}_0)=0.025$ where the full spectrum is delocalized. Top Right Panel: Plot of N_{0j} as a function of j/L for $\omega_D/(\pi\mathcal{J}_0)=0.175$ at which there is a mobility edge between delocalized and multifractal states. Middle Left Panel: Plot of N_{0j} as a function of j/L for $\omega_D/(\pi\mathcal{J}_0)=0.20$ at which there is a mobility edge between delocalized and localized states. Middle Right Panel: Plot of N_{0j} as a function of j/L for $\omega_D/(\pi\mathcal{J}_0)=0.24$ at which there is a mobility edge between delocalized and multifractal states. This drive frequency is near the critical frequency ω_c . Bottom left Panel: Plot of N_{0j} as a function of j/L for $\omega_D/(\pi\mathcal{J}_0)=0.5$ where the full spectrum is localized. Bottom right Panel: Plot of the number of particles present in the right half (beginning from domain wall initial state) as a function of number of drive cycles n_0 for various representative drive frequencies. All other parameters are same as in Fig. 1. See text for details.

Appendix B: Approach to Steady state

In this appendix we discuss, in brief, the approach of our model subjected to square pulse drive, to the steady states shown in the main text, starting from the domain wall initial state given by,

$$|\psi_{\text{init}}\rangle = |n_1 = 1, \dots, n_{L/2} = 1, n_{L/2+1} = 0, \dots, n_L = 0\rangle$$

To this effect we study the distribution of fermion number density $N_j = \langle \psi(n_0 T) | \hat{n}_j - 1/2 | \psi(n_0 T) \rangle$, where $\psi(n_0 T) = U(n_0 T, 0) |\psi_{\text{init}}\rangle$ and $\hat{n}_j = c_j^\dagger c_j$ at different number of cycles n_0 . Fig. 15 shows the distributions studied for different drive frequencies. For low drive frequencies ($\omega_D/(\pi\mathcal{J}_0) = 0.025$) where the entire spectrum was shown to be delocalized, it is seen that this quantity attains its steady state value for a smaller number of cycles compared to other cases. As the drive frequency is increased and we reach the region with mobility edge, transport becomes slower as can be seen from the

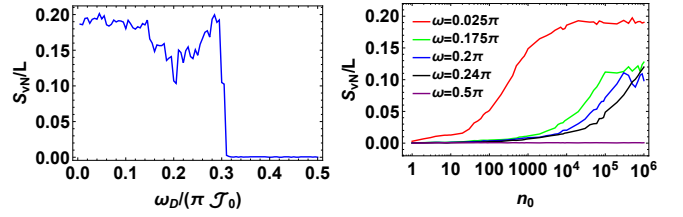


FIG. 16: Left panel: Plot of half chain von-Neumann entanglement entropy (S_{vN}) in the steady state starting from a domain wall initial state scaled by the system length L as a function of drive frequency $\omega_D/(\pi\mathcal{J}_0)$ showing the signature of delocalized, localized and mixture of delocalized and multifractal and delocalized and localized states. Right Panel: Plot of half chain entanglement as a function of number of drive cycles n_0 for various representative drive frequencies showing how it reaches the steady state value. All other parameters are same as in Fig. 1.

top right and middle left panels which show results for $\omega_D/(\pi\mathcal{J}_0) = 0.175$ and $\omega_D/(\pi\mathcal{J}_0) = 0.20$ respectively. However, it is seen that while 10^3 drive cycles is not enough to reach close to the steady states, 10^4 cycles is enough even for the drive frequency ($\omega_D/(\pi\mathcal{J}_0) = 0.20$) which supports a mobility edge between localized and delocalized states. However for a drive frequency higher than that which also supports multifractal and delocalized states ($\omega_D/(\pi\mathcal{J}_0) = 0.24$), $n_0 = 10^4$ gives the impression the system is localized from the distribution. Only at extremely large number of cycles $n_0 = 10^5$ does the system give the expected behavior of the steady state. This is possibly due to the proximity of this drive frequency to the critical frequency $\omega_D/(\pi\mathcal{J}_0) = 0.30$. The bottom right panel of Fig. 15 shows the evolution of $N_h = \sum_{j=L/2+1}^L \hat{n}_j$ with time, i.e., the transport of particles from the left-half of the system to the right-half. It also shows that only after a sufficiently long time scale does N_h for $\omega_D/(\pi\mathcal{J}_0) = 0.24$ overtake $\omega_D/(\pi\mathcal{J}_0) = 0.20$ which is expected in the steady state as the latter frequency supports delocalized and localized eigenfunctions and hence, particle transport should show a suppression compared to the former drive frequency which supports delocalized and multifractal eigenfunctions.

In Fig. 16 we study whether similar feature show up in the half chain entanglement entropy of the system starting from the domain wall state. To calculate the stroboscopic time evolution of von-Neumann entropy we first calculate the time-evolution of the two-point correlation function ($\langle c_i^\dagger c_j \rangle(t)$) in the Heisenberg picture, and then use the technique outlined in Ref. 30 to extract the von-Neumann entropy between the left half of the system (between sites 1 and $L/2$) and the right half ($L/2 + 1$ and L). To calculate the steady state entanglement entropy, we utilize the steady state correlators calculated using the procedure outlined in the main text and then use the method of Ref. 30. The steady state entanglement shows the expected features of a dip when the system's eigenstates change from being fully delocalized

to delocalized and multifractal and then, to delocalized and localized as the drive frequency is increased from $\omega_D \approx 0$. Finally, the steady state entanglement becomes almost zero when the system becomes fully localized beyond ω_c . However, as with the number density in the

right-half of the system, the entanglement also requires larger times to approach its steady state value as we tune the drive frequency to be closer to the critical frequency, showing a behavior similar to the transport of particles to the right half of the system.

-
- ¹ S. Aubry and G. Andre, Ann. Isr. Phys. Soc. **3**, 133 (1980); M. Ya. Abzel, Sov. Phys. JETP **17**, 665 (1963); M. Ya. Abzel, *ibid.* **19**, 634 (1964); M. Ya Abzel, Phys. Rev. Lett. **43**, 1954 (1979).
- ² J. Biddle, B. Wang, J. D. J. Priour, and S. D. Sarma, Phys. Rev. A, **80**, 021603(R) (2009); D. J. Boers, B. Goedeke, D. Hinrichs, and M. Holthaus, Phys. Rev. A, **75**, 063404 (2007); R. Riklund, Y. Liu, G. Wahlstrom, and Z. Zhao-bo, J. Phys. C: Solid State Phys., **19**, L705 (1986); F. A. B. F. de Moura, A. V. Malyshev, M. L. Lyra, V. A. Malyshev, and F. Dominguez-Adame, Phys. Rev. B, **71**, 174203 (2005); A. V. Malyshev, V. A. Malyshev, and F. Dominguez-Adame, Phys. Rev. B, **70**, 172202 (2004); S.-J. Xiong and G.-P. Zhang, Phys. Rev. B, **68**, 174201 (2003); A. Rodriguez, V. A. Malyshev, G. Sierra, M. A. Martín-Delgado, J. Rodríguez-Laguna, and F. Domínguez-Adame, Phys. Rev. Lett. **90**, 027404 (2003); S. Das Sarma, A. Kobayashi, and R. E. Prange, Phys. Rev. Lett. **56**, 1280 (1986); J. Biddle and S. Das Sarma, Phys. Rev. Lett. **104**, 070601 (2010).
- ³ X. Deng, S. Ray, S. Sinha, G. V. Shlyapnikov, and L. Santos, Phys. Rev. Lett. **123**, 025301 (2019).
- ⁴ D-L Deng, S. Ganeshan, X. Li, R. Modak, S. Mukerjee, and J. H. Pixley, Ann. Phys. **529**, 1600399 (2017); A. Jagannathan, arXiv:2012.14744 (unpublished).
- ⁵ G. Roati, C. D. Errico, L. Fallani, M. Fattori, C. Fort, M. Zaccanti, G. Modugno, M. Modugno, and M. Inguscio, Nature (London) **453**, 895 (2008); B. Deissler, M. Zaccanti, G. Roati, C. D. Errico, M. Fattori, M. Modugno, G. Modugno, and M. Inguscio, Nat. Phys. **6**, 87 (2010).
- ⁶ M. Schreiber, S. S. Hodgman, P. Bordia, H. P. Lüschen, M. H. Fischer, R. Vosk, E. Altman, U. Schneider, and I. Bloch, Science **349**, 842 (2015); H. P. Lüschen, P. Bordia, S. Scherg, F. Alet, E. Altman, U. Schneider, and I. Bloch, Phys. Rev. Lett. **119**, 260401 (2017).
- ⁷ P. W. Anderson, Phys. Rev. **109**, 1492 (1958); E. Abrahams, P. W. Anderson, D. C. Licciardello, and T. V. Ramakrishnan, Phys. Rev. Lett. **42**, 673 (1979); P. A. Lee and T. V. Ramakrishnan Rev. Mod. Phys. **57**, 287 (1985).
- ⁸ A. Polkovnikov, K. Sengupta, A. Silva, and M. Vengalattore, Rev. Mod. Phys. **83**, 863 (2011); J. Dziarmaga, Adv. Phys. **59**, 1063 (2010); J. Dziarmaga, Adv. Phys. **59**, 1063 (2010); A. Dutta, G. Aeppli, B. K. Chakrabarti, U. Divakaran, T. F. Rosenbaum, and D. Sen, *Quantum phase transitions in transverse field spin models: from statistical physics to quantum information* (Cambridge University Press, Cambridge, 2015); S. Mondal, D. Sen and K. Sengupta, *Non-equilibrium dynamics of quantum systems: order parameter evolution, defect generation, and qubit transfer*, Lect. Notes Phys. **21** 802 (2010).
- ⁹ L D'Alessio, Y Kafri, A Polkovnikov, M Rigol Advances in Physics **65**, 239 (2016); L. D'Alessio and A. Polkovnikov, Ann. Phys. **333**, 19 (2013).
- ¹⁰ T. Kitagawa, E. Berg, M. Rudner, and E. Demler, Phys. Rev. B **82**, 235114 (2010); N. H. Lindner, G. Refael, and V. Galitski, Nat. Phys. **7**, 490 (2011); T. Kitagawa, T. Oka, A. Brataas, L. Fu, and E. Demler, Phys. Rev. B **84**, 235108 (2011); M Thakurathi, A. A Patel, D Sen, and A Dutta Phys. Rev. B **88**, 155133 (2013); A Kundu, HA Fertig, B Seradjeh, Phys. Rev. Lett. **113**, 236803 (2014); F. Nathan and M. S. Rudner, New J. Phys. **17** 125014 (2015); B. Mukherjee, A. Sen, D. Sen, and K. Sengupta, Phys. Rev. B **94**, 155122 (2016); B. Mukherjee, P. Mohan. D. Sen, and K. Sengupta, Phys. Rev. B **97**, 205415 (2018); B. Mukherjee, Phys. Rev. B **98**, 235112 (2018).
- ¹¹ For a review, see M. Heyl, Rep. Prog. Phys. **81**, 054001 (2018); M. Heyl A. Polkovnikov, and S. Kehrein Phys. Rev. Lett. **110**, 135704 (2013).
- ¹² A. Sen, S. Nandy, and K. Sengupta, Phys. Rev. B **94**, 214301 (2016); S. Nandy, K. Sengupta, and A. Sen, J. Phys. A: Math. Theor. **51**, 334002 (2018).
- ¹³ A. Das, Phys.Rev. B **82**, 172402 (2010); S. Bhattacharyya, A. Das, and S. Dasgupta, Phys. Rev. B **86**, 054410 (2012); S. S. Hegde, H. Katiyar, T. S. Mahesh, and A. Das, *ibid.* **90**, 174407 (2014).
- ¹⁴ S. Mondal, D. Pekker, and K. Sengupta, Europhys. Lett. **100**, 60007 (2012); U. Divakaran and K. Sengupta, Phys. Rev. B **90**, 184303 (2014); S. Kar, B. Mukherjee, and K. Sengupta, Phys. Rev. B **94**, 075130 (2016); S. Lubini, L. Chirondojan, G. Oppo, A. Politi, and P. Politi, Phys. Rev. Lett. **122**, 084102 (2019); B. Mukherjee, A. Sen, D. Sen, and K. Sengupta, Phys. Rev. B **102**, 075123 (2020).
- ¹⁵ V. Khemani, A. Lazarides, R. Moessner, and S. L. Sondhi, Phys. Rev. Lett. **116**, 250401 (2016).
- ¹⁶ J. Zhang, P. W. Hess, A. Kyprianidis, P. Becker, A. Lee, J. Smith, G. Pagano, I-D. Potirniche, A. C. Potter, A. Vishwanath, N. Y. Yao, and C. Monroe, Nature **543**, 217 (2017); D. V. Else, B. Bauer, and C. Nayak, Phys. Rev. Lett. **117**, 090402 (2016).
- ¹⁷ B. Mukherjee, S. Nandy, A. Sen, D. Sen, and K. Sengupta, Phys. Rev. B **101**, 245107 (2020); B. Mukherjee, A. Sen, D. Sen, and K. Sengupta, Phys. Rev. B **102**, 014301 (2020).
- ¹⁸ S. Nandy, A. Sen, and D. Sen, Phys. Rev. X **7**, 031034 (2017); S. Nandy, A. Sen, and D. Sen, Phys. Rev. B **98**, 245144 (2018).
- ¹⁹ A Lazarides, A Das, R. Moessner, Phys. Rev. E **90**, 012110 (2014); A. Russomanno, A. Silva, and G. E. Santoro Phys. Rev. Lett. **109**, 257201 (2012).
- ²⁰ M. Bukov, L. D'Alessio, and A. Polkovnikov, Adv. Phys. **64** 139 (2015); A. Sen, D. Sen, and K. Sengupta, arXiv:2102.00793 (unpublished); S. Blanes, F. Casas, J. A. Oteo, and J. Ros, Physics Reports **470**, 151 (2009); G. Floquet, Gaston Annales de l'Ecole Normale Supérieure, **12**, 47 (1883).
- ²¹ A. Soori and D. Sen, Phys. Rev. B **82**, 115432 (2010); T. Bilitewski and N. R. Cooper, Phys. Rev. A **91**, 033601 (2015).
- ²² R. Ghosh, B. Mukherjee, and K. Sengupta, Phys. Rev. B

- 102**, 235114 (2020); M. Bukov, M. Kolodrubetz, and A. Polkovnikov, Phys. Rev. Lett. **116**, 125301 (2016).
- ²³ F. Wegner, Z. Phys. B **36**, 209 (1980); H. Aoki, Phys. Rev. B **33**, 7310 (1986); B.L. Altshuler, V.E. Kravtsov, and I.V. Lerner, JETP Lett. **43**, 441 (1986); A. D. Mirlin, Y. V. Fyodorov, A. Mildenerger, and F. Evers, Phys. Rev. Lett. **97**, 046803 (2006);
- ²⁴ M. Janssen, Phys. Rep. **295**, 1 (1998); F. Evers and A. D. Mirlin, Rev. Mod. Phys. **80**, 1355 (2008).
- ²⁵ S.J. Garratt J.T. Chalker, arXiv:2012.11580
- ²⁶ S. Roy, I. M. Khyamovich, A. Das, and R. Moessner, Sci-post Phys. **4**, 025 (2018).
- ²⁷ S. Ray, A. Ghosh, and S. Sinha Phys. Rev. E **97**, 010101(R) (2018).
- ²⁸ T. Antal, Z. Racz, A. Rakos, and G.M. Schutz, Phys. Rev. E **59**, 4912 (1999); T. Antal, P. L. Krapivsky, and A. Rákos, Phys. Rev. E **78**, 061115 (2008); V. Eisler and Z. Racz, Phys. Rev. Lett. **110**, 060602 (2013); V. Hunyadi, Z. Racz, and L. Sasvari, Phys. Rev. E **69**, 066103 (2004); R. Ghosh and A. Das, Phys. Rev. B **103**, 024202 (2021); B. Mukherjee, K. Sengupta and S. N. Majumdar Phys. Rev. B **98**, 104309 (2018).
- ²⁹ L. F. Santos and M. Rigol, Phys. Rev. E **81**, 036206 (2010); L. F. Santos and M. Rigol, *ibid* **82**, 031130 (2010); L. D'Alessio and M. Rigol, Phys. Rev. X **4**, 041048 (2014).
- ³⁰ S-A Cheong and C.L. Henley, Phys. Rev. B **69**, 075111 (2004)